



This is a repository copy of *Exploiting thermal strain to achieve an in-situ magnetically graded material*.

White Rose Research Online URL for this paper:
<http://eprints.whiterose.ac.uk/138442/>

Version: Published Version

Article:

Freeman, F.S.H.B. orcid.org/0000-0002-7402-1790, Lincoln, A., Sharp, J. et al. (2 more authors) (2019) Exploiting thermal strain to achieve an in-situ magnetically graded material. *Materials and Design*, 161. pp. 14-21. ISSN 0261-3069

<https://doi.org/10.1016/j.matdes.2018.11.011>

Reuse

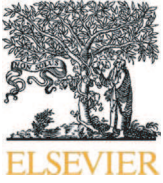
This article is distributed under the terms of the Creative Commons Attribution (CC BY) licence. This licence allows you to distribute, remix, tweak, and build upon the work, even commercially, as long as you credit the authors for the original work. More information and the full terms of the licence here:
<https://creativecommons.org/licenses/>

Takedown

If you consider content in White Rose Research Online to be in breach of UK law, please notify us by emailing eprints@whiterose.ac.uk including the URL of the record and the reason for the withdrawal request.



eprints@whiterose.ac.uk
<https://eprints.whiterose.ac.uk/>



Exploiting thermal strain to achieve an in-situ magnetically graded material

Felicity S.H.B. Freeman^{a,*}, Alex Lincoln^b, Jo Sharp^a, Al Lambourne^c, Iain Todd^a

^a Department of Materials Science & Engineering, University of Sheffield, Sheffield S1 3JD, UK

^b The NEST Research Group, School of Computer Science, The University of Manchester, Oxford Road, Manchester M13 9PL, UK

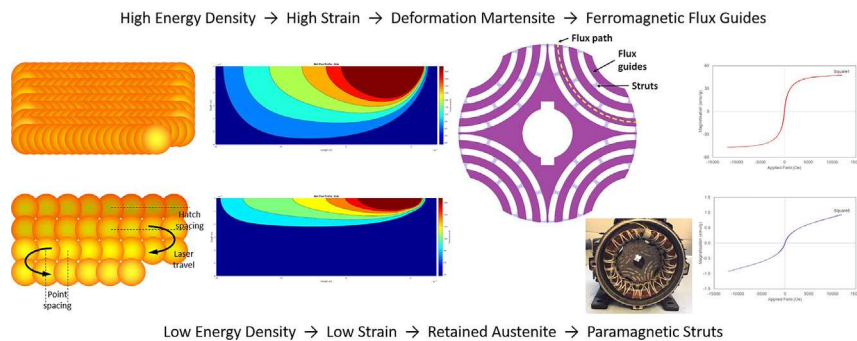
^c Rolls-Royce plc, Derby DE24 8BJ, UK



HIGHLIGHTS

- A fully austenitic structure was retained in 17-4PH by using the fine grain size to completely suppress thermally-driven martensite
- Strain accrued during the build was used to trigger and control the extent of deformation-driven martensitic transformation
- The effect was shown to be sensitive to both build parameters and sample geometry
- A magnetically-graded single-composition material was built by tailoring the ratio of ferromagnetic martensite to paramagnetic austenite
- This was exploited to build a magnetically graded rotor which was run in a synchronous motor

GRAPHICAL ABSTRACT



ARTICLE INFO

Article history:

Received 12 August 2018

Received in revised form 1 October 2018

Accepted 5 November 2018

Available online 08 November 2018

Keywords:

Selective laser melting (SLM)
Functionally graded material (FGM)
Magnetic grading
Martensitic transformation
Deformation martensite
Thermal strain

ABSTRACT

Spatially resolved functional grading is a key differentiator for additive manufacturing, achieving a level of control that could not be realised by conventional methods. Here we use the rapid solidification and thermal strain associated with selective laser melting to create an in-situ microstructurally and magnetically graded single-composition material, exploiting the solid-state austenite-martensite phase transformation. The fine grain sizes resulting from high cooling rates suppress the thermal martensite start temperature, increasing the proportion of retained austenite. Then the thermal strain accrued during the build causes in-situ deformation-driven martensitic transformation. By controlling the thermal strain, through appropriate selection of build parameters and geometry, we have been able to control the final ratio of austenite to martensite. Fully austenitic regions are paramagnetic, while dual-phase regions show increasingly ferromagnetic behaviour with an increasing proportion of martensite. We exploit this to build a magnetically graded rotor which we run successfully in a synchronous motor.

© 2018 The Authors. Published by Elsevier Ltd. This is an open access article under the CC BY license (<http://creativecommons.org/licenses/by/4.0/>).

1. Introduction

The solid-state transformation from austenite to martensite is accompanied by a change in magnetic response from paramagnetic to

* Corresponding author.

E-mail address: fshfreeman1@sheffield.ac.uk (F.S.H.B. Freeman).

Table 1
Build parameters.

Build	Power W	Exposure μs	Point μm	Speed mm s^{-1}	Layer μm	Hatch μm	ϵ^*	E^*
S1	200	100	30	280	40	30	1.00	23.7
S2	200	100	34	314	40	34	0.84	19.7
S3	200	100	40	364	40	40	0.77	16.3
S4	200	100	52	461	40	52	0.60	11.4
S5	200	100	90	738	40	90	0.33	5.3

ferromagnetic. This gives scope for building an in-situ magnetically graded material from a single alloy composition by selectively allowing or suppressing martensitic transformation.

The martensite start temperature, M_s , of 17-4PH stainless steel is reported to be 105–132 °C [1,2]. Conventionally processed 17-4PH is primarily martensitic at room temperature, with <10 wt% retained austenite [2,3]. However, 17-4PH built by selective laser melting (SLM) has been reported to retain a much higher proportion of austenite, up to 80 wt% [4–8]. This has been attributed to rapid solidification driving fine austenite grain size, which in turn suppresses M_s , [9–11]. This effect has been seen in other techniques with similar rapid solidification rates (10^5 – 10^6 K s^{-1}) [12–14], including splat quenching [15], and melt spinning [16].

Thermal strain is a common issue with additively manufactured (AM) parts, due to the extreme thermal gradients caused by rapid melting and solidification [17]. These can cause distortion of the final component [18], but could also drive phase transformation in a susceptible alloy. It has been demonstrated that SLM-built 17-4PH can exhibit transformation induced plasticity (TRIP), where metastable retained austenite transformed to martensite under applied deformation [4].

The solidification conditions of SLM-built 17-4PH are expected to significantly stabilise austenite, potentially to the extent of retaining a fully austenitic structure. Thermal strain is normally regarded as an undesirable aspect of additively manufactured components, but, if it can be controlled through selection of build parameters, it may be possible to use this to control the extent of deformation-driven martensitic transformation and therefore produce a microstructurally and magnetically graded single-composition material.

Functional grading is a significant area of interest within additive manufacture (AM), with studies already demonstrating grading for composition [19], precipitate density [20], grain size [21] and twinning [22]. Magnetic grading is an enabling technology for electrical machine architectures, including switched reluctance motors [23] and internal permanent magnet machines, but specifically for synchronous reluctance motors [24,25].

Synchronous reluctance motors pass current through stator windings to set up a rotating magnetic field. The rotor locks into this field and is pulled round by it at the same speed (synchronous). The rotor

consists of radial shells of ferromagnetic flux guides, separated by insulating (non-magnetic) gaps that constrain the flux within the guides. The shells require support struts for mechanical integrity, but these can act as flux leakage paths, reducing efficiency.

The rotors are currently manufactured by punching slices from thin sheets of ferromagnetic electrical steel which are laminated into a stack. The support struts holding the shells together are therefore made of the same ferromagnetic steel, so their width must be minimised to reduce flux leakage. One alternative is to build rotors by axial lamination but this is difficult to manufacture [26]. Another option is powder sintering, using powders of two compositions [27]. Using AM to functionally grade during build gives the opportunity to achieve magnetic variation from a single alloy composition with a high level of spatial resolution.

2. Modelling

Steels built by SLM are characterised by an austenite grain size of 10–100 μm , where the grains contain a forest of elongated solidification cells, 0.5–2 μm in diameter [7,28–30]. These cells are surrounded by dense dislocation walls which exert their own strain field [31]. The dislocation walls are geometrically necessary to accommodate the slight orientation mismatch between adjacent cells [32]. The cell size is determined by the solidification conditions [33–36], so this uniformity of cell size suggests that solidification conditions are relatively consistent across a range of build parameters and alloy chemistry.

A relationship has been established between austenite grain size and M_s for a range of steel compositions [9]. This indicates that a grain size of <10 μm would suppress M_s below room temperature in 17-4PH, giving a fully austenitic structure (Appendix A). A grain size of 100 μm would have a lesser effect, suppressing M_s to around 40 °C, giving a structure with 80 vol% retained austenite [3].

To predict the thermal behaviour, we modelled the melt pool in Matlab. The model was based on the Eagar solution for a continuously moving Gaussian beam [37], modified to apply to a pulsed laser, include the residual heat from previous hatches and account for the latent heat of melting within the melt pool. From this we were able to predict the melt pool geometry and the solidification rate behind the laser beam.

The model was validated against melt tracks built for a range of power at constant exposure time (100 μs) and point spacing (30 μm). The melt tracks showed keyhole-mode melting at higher power, allowing a scaling factor to be determined to predict the melt depth in keyhole-mode from a conduction-mode model [38,39]. The baseline conduction-mode absorptivity was taken to be 45%, based on the absorptivity for 316SS under similar conditions [40].

Eq. (1) describes the relationship between primary dendrite arm spacing, λ_1 , and cooling rate, \dot{T} , where a and n are material dependent constants. For steels, a is quoted in the range 60–100 and n between 0.2 and 0.5 [33–35]. This was originally validated for processes with cooling rates of 10^{-2} – 10^2 K s^{-1} , and becomes increasingly sensitive to

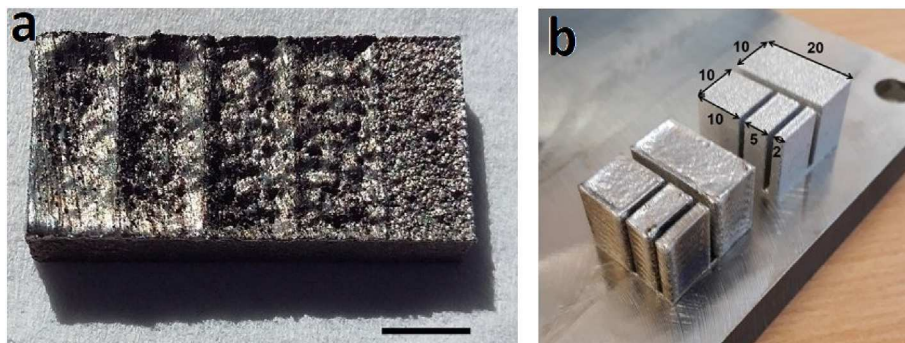


Fig. 1. a) Graded cuboidal sample, with 4 mm thick slices for each build condition from high energy density (left) to low energy density (right). Scale bar is 4 mm. b) Samples with different cross-sectional areas built to S1 (bottom left) and S5 (top right) conditions. Measurements shown in mm.

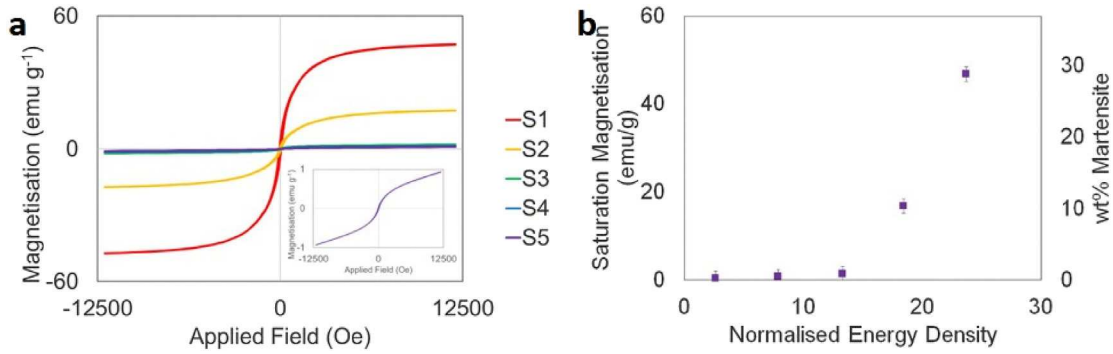


Fig. 2. Magnetic characterisation. (a) VSM hysteresis loops for Square Series with inset of individual data for low energy density (S5) sample. (b) Phase fraction martensite determined from VSM saturation magnetisation for Square, Hatch and Point Series. Error bars show standard error.

experimental error at higher cooling rates so is only used here for guidance [13].

$$\lambda_1 = a \dot{T}^{-n} \quad (1)$$

For the range of build parameters achievable with the Renishaw SLM125, the melt pool model predicted cooling rates in the range 10^4 – 10^6 K s⁻¹. Even at the lower end of this range, using extremely high energy density, the melt pool would solidify in a cellular mode with $\lambda_1 \approx 5$ μ m. For more normal build conditions (200 W, 1000 m s⁻¹), the predicted λ_1 was only 1 μ m, consistent with the diameters reported in the literature.

While this predicts solidification cell size rather than grain size, martensite growth has been observed to stop at sub-grain boundaries, where material with similar crystal orientation was separated by dense dislocation walls [41]. This structure is comparable with the solidification cells, indicating that they can also play a role in suppressing transformation. A solidification cell size of <5 μ m would suppress M_s below room temperature and give a fully austenitic structure.

There is the potential for coarsening driven by in-situ heat treatment from the laser passing on subsequent hatches and layers [42,43]. The model predicted this heat treatment to be equivalent to <18 s at 800 °C for the highest energy density (S1) condition, and shorter for all other conditions. For comparison, heat treatment of SLM-built 316L at 800 °C for 6 min showed only a slight reduction in dislocation density around the solidification cells, and no cell coarsening [28]. It was therefore judged unlikely that in-situ heat treatment would modify the grain and cell size sufficiently to change the extent of thermally-driven transformation.

The model was then used to predict the potential for thermal strain, using the dimensionless thermal deformation parameter [44], ε^* . This is shown in Eq. (2) in a simplified form for a fixed material, assuming deposition time to be determined by the average scan speed v , hatch spacing h and sample area A . The other parameters are laser power Q , melt pool length w and second moment of inertia of the substrate I .

$$\varepsilon^* = \frac{A w}{I h} \left[\frac{Q}{v} \right]^{3/2} \quad (2)$$

The results showed that, for a fixed geometry, it was possible to vary the strain parameter by over 500 \times by changing the build parameters. However, ε^* is a normalised parameter, so without calibration it was not possible to assess whether this would be sufficient variation to give a measurable change in martensite phase fraction.

3. Experimental method

Two series of builds were designed, one covering a range of energy density, E^* , at fixed geometry (Table 1) and the other covering a range of geometries at fixed energy density. The chemical composition of

the 17-4PH powder is available in Supplementary Table 1. SEM images of the powder and the particle size distribution are available in Supplementary Fig. 1.

All samples were built using a Renishaw SLM125 under argon. Samples were built using a meander scan strategy with 67° rotation between layers. The samples were removed from the baseplate using electro-discharge machining (EDM) to minimise unintended deformation.

A set of cylinders (8 mm ϕ \times 10 mm height) were built for each of the S1–S5 conditions for individual characterisation. A graded cuboid was built from 4 mm wide blocks of each condition ordered in decreasing energy density, with grading in the build plane so the different conditions were built simultaneously (Fig. 1a). To improve bonding between the interfaces, the stereolithography (STL) files for each individual condition were overlapped by 0.1 mm.

The S1 and S5 conditions were also used to build a set of samples with different cross-sectional areas in the build plane (Fig. 1b). All samples were 15 mm in height, and 10 mm in width, but ranged from 2 mm to 20 mm in length. These samples were EDM wire-cut into slices, 1 mm in thickness, working from the top surface towards the baseplate.

A handheld magnet was used to test the graded sample before removal from the baseplate. This was intended for qualitative assessment of the true as-built condition, in case of unintended deformation during removal.

Magnetic characterisation was carried out on 1.5 mm thick discs cut by EDM from the top of the cylindrical samples of each condition from Table 1. The vibrating sample magnetometer (VSM) was a MicroSense Model 10 at the University of Manchester. The results were normalised against the sample mass. All measurements were carried out with the field perpendicular to the build direction. The measurement program is detailed in Supplementary Table 2.

Feritscope measurements were made using a Fischer Feritscope MP30 at PTS (TQM) Ltd. Measurements were made on 2 mm thick

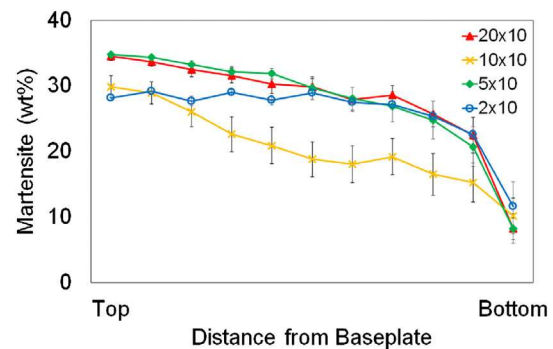


Fig. 3. Feritscope measurements from high energy density (S1) samples of different cross-sections showing increasing martensite content with distance from the build plate, total height 15 mm. Error bars show standard error.

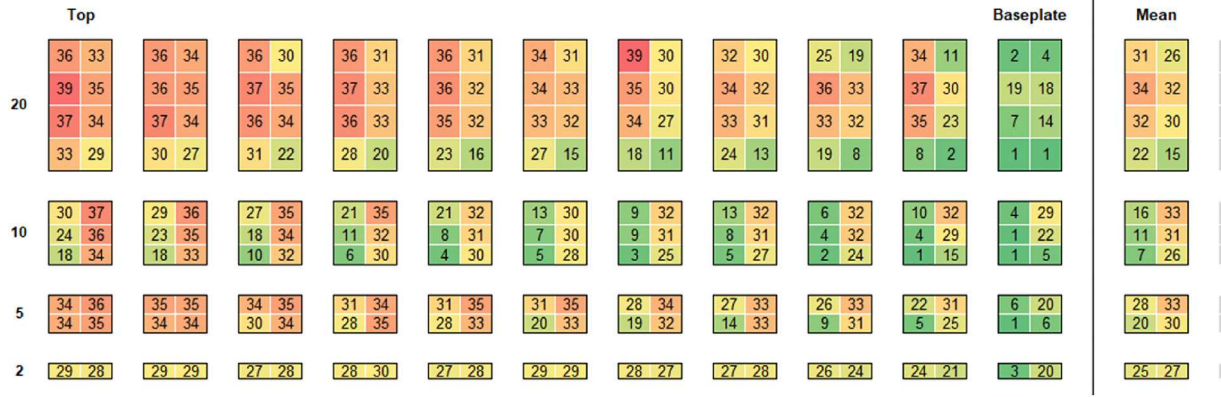


Fig. 4. Feritscope measurements from high energy density (S1) samples of different cross-sections showing variation in martensite content across each slice for each geometry.

discs cut from the cylinders, below the discs used for VSM. Four measurements were taken and averaged for each of the samples. Measurements were also taken from all of the slices of the samples with different cross-sectional area (Fig. 1b).

X-ray diffraction (XRD) was carried out on the discs previously used for Feritscope measurement, using a PANalytical X’Pert³ Powder with Cu K α radiation at a step size of 0.0394° and 5000 s per step. Data from sections corresponding to the four major austenite peaks were deconvoluted in Origin using the ‘Peak Analyzer’ approach, with either a Gaussian or Gauss-Lorentz curve fitting (Supplementary Fig. 2). The peak positions were used to calculate average lattice parameters (Supplementary Fig. 3).

Scanning electron microscopy (SEM) was carried out on a FEI Nova FEGSEM at the University of Sheffield, operating at 20 kV. The images were taken from a vertical section (perpendicular to the build plane) through the graded cuboid. The sample was ground and polished, then etched with Kallings #2 reagent.

4. Results

4.1. Graded sample

Using a handheld magnet, we found that the cuboidal sample manufactured with graduated 4 mm thick slices of the five conditions (Fig. 1a) successfully demonstrated an in-situ magnetically graded response, from magnetic (ferromagnetic) at the high energy density (S1) end to non-magnetic (paramagnetic) at the low energy density (S5) end. This was confirmed both before and after removal from the baseplate.

4.2. Magnetic characterisation - VSM

The high energy density sample (S1) showed a soft ferromagnetic response with some paramagnetic material contribution evident at

high applied field (Fig. 2a). The intermediate conditions showed decreasing ferromagnetic behaviour with decreasing energy density. For the low energy density (S5) condition the behaviour was majority paramagnetic, with only a small ferromagnetic contribution (Fig. 2a inset). The individual hysteresis loops are shown in Supplementary Fig. 4.

We selected the saturation magnetisation, m_s , to assess magnetic behaviour because it is a structure independent characteristic, unaffected by porosity or dislocations, and follows a rule-of-mixtures from the values for the individual phases present [45]. Assuming a two-phase structure and given that austenite is paramagnetic and that martensite is ferromagnetic with saturation magnetisation $m_{s\alpha'}$, the fraction of martensite $f_{\alpha'}$ and austenite f_{γ} are given by Eqs. (3) and (4) [45].

$$f_{\alpha'} = \frac{m_s}{m_{s\alpha'}} \quad (3)$$

$$f_{\gamma} = 1 - f_{\alpha'} \quad (4)$$

The saturation magnetisation of fully martensitic low sulphur 17-4PH is 162.4 emu g⁻¹ [46]. We used emu g⁻¹ throughout because it was consistent with wt% and avoided porosity corrections.

Our analysis showed the high energy density (S1) sample contained 29 wt% martensite and 71 wt% austenite (Fig. 2b). With reducing energy density, the proportion of martensite reduced and that of austenite increased. The low energy density sample (S5) contained >99.5 wt% austenite and <0.5 wt% martensite. Additional scans of the S1 sample showed repeatability within 1 wt%.

4.3. Magnetic characterisation - Feritscope

Feritscope measurements were used to give spatially resolved phase information for the samples with different cross sections (Fig. 1b). For the high energy density (S1) condition, all geometries showed martensite content increasing with distance from the baseplate (Fig. 3).

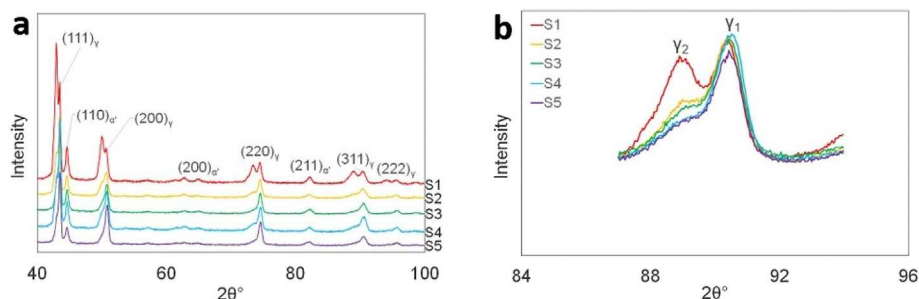


Fig. 5. Phase identification from XRD. A) XRD traces for all build conditions with main austenite and martensite peaks indicated. b) Detail of two austenite phases for (311) reflection.

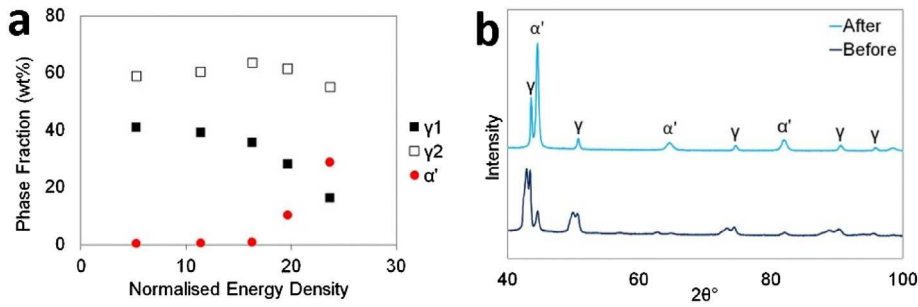


Fig. 6. Investigation of γ_1 and γ_2 . a) Quantitative phase analysis showing relative phase fractions of two austenite phases and martensite phase with energy density. b) XRD showing effect of manual polishing (sample preparation) on intensity of austenite and martensite peaks.

Different samples had different levels of martensite, possibly influenced by both sample area and aspect ratio and their relative effects on deposition time and sample rigidity (second moment of inertia). The low energy density (S5) samples all showed a fully austenitic structure throughout the build.

The data for the high energy density (S1) condition also showed variation across each geometry, with one side showing a generally higher martensite content (Fig. 4).

4.4. Phase identification

XRD confirmed that all samples had a dual phase martensite/austenite structure (Fig. 5a). The traces showed a double austenite peak indicating that two different austenite phases (γ_1 and γ_2) were present (Fig. 5b). The material showed crystallographic texture, so was not suitable for Rietveld analysis. Instead, we deconvoluted sections of the data in Origin to extract the peak positions and areas for the two austenite phases independently (Supplementary Fig. 2).

Assuming γ_1 and γ_2 to have the same structure factor, the peak areas were used to determine the relative fraction of the two austenite phases. This was combined with the VSM data for the phase fraction of martensite, to show that the fraction of γ_2 was constant with increasing energy density, while that of γ_1 decreased and α' -martensite increased (Fig. 6a).

Using the peak positions, we were able to calculate the lattice parameters for the two austenite phases (Supplementary Fig. 3). The lattice parameter for the γ_1 phase (3.60 Å) corresponded well with that expected

from the bulk composition, while that for the γ_2 phase (3.64 Å) was shifted by about 1%, and the shift was constant across the range of energy densities.

The XRD data shown in Fig. 5 was carried out on the EDM cut surface without polishing or other preparation. This was done to avoid additional martensitic transformation caused by deformation during surface preparation. One sample was then manual polished and re-scanned (Fig. 6b), and polishing was seen to completely remove the γ_2 reflections, with an associated increase in intensity of the martensite peaks.

4.5. Microstructure

Examination by SEM showed comparable microstructures across all build conditions, with a forest of solidification cells ranging from 0.5 μm to 2 μm (Fig. 7). There was no trend in solidification cell size with energy density. Further, the SEM also showed all samples to have grains between 10 μm and 20 μm (Fig. 8). Additional SEM images showed no trend in grain size or solidification cell size with depth through the sample in the build direction (Supplementary Fig. 5).

4.6. Synchronous motor

The synchronous rotor was designed to replace the rotor from an off-the-shelf TEC 0.12 kW 4 pole 3 phase AV induction motor, model 56M4C-TECA. It was built in three 15 mm high sections, using the high energy density (S1) condition for ferromagnetic flux guides and low energy density (S5) condition for the paramagnetic struts

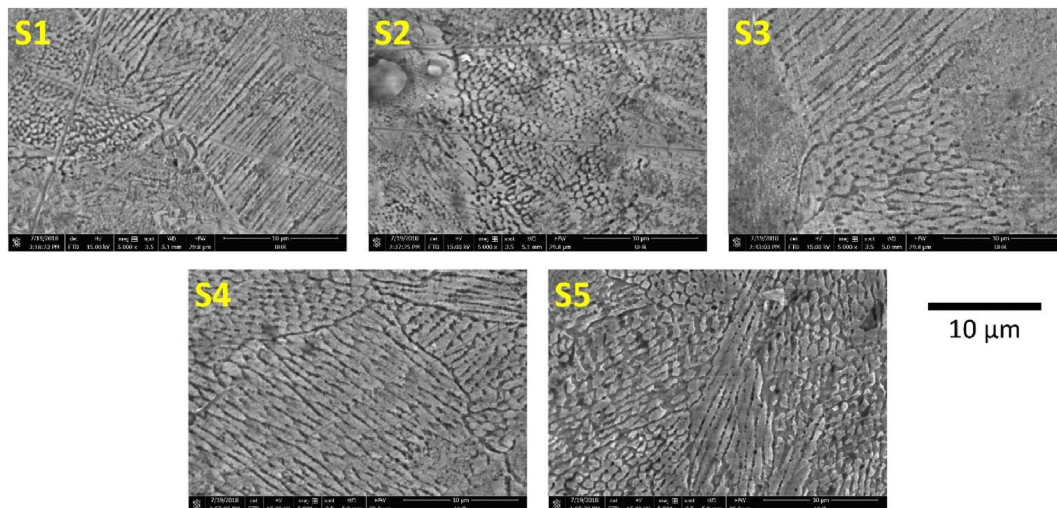


Fig. 7. SEM of all build conditions showing solidification cells. Build direction is vertical. Scale bar is 10 μm .

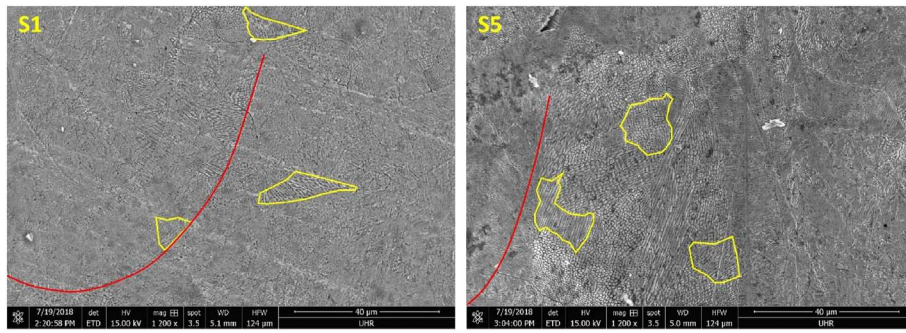


Fig. 8. SEM of high energy density (S1) and low energy density (S5) build conditions showing comparable grain sizes. A few grains are highlighted in yellow for clarity. The edge of the melt pool is highlighted in red. Build direction is vertical. Scale bar is 40 μm . (For interpretation of the references to color in this figure legend, the reader is referred to the web version of this article.)

(Fig. 9a). Due to the complexity of the geometry, the STL files for the individual conditions were not overlapped as they had been for the cuboidal graded samples.

The rotor showed slight cracking at the interfaces between the different build conditions, which precluded high-speed testing. The cracks were filled with resin, and then the rotor was mounted on a shaft with rolling element bearings and assembled into the motor (Fig. 9b). After tuning the motor drive, it was run at 100, 200, 300 and 400 rpm. Current probes were attached to measure the pulse width modulated (PWM) supply from the drive electronics (Fig. 9c). While not an optimised design, the machine performed as expected at low speeds.

5. Discussion

The primary aim of this study was to create an in-situ magnetically graded microstructure by suppressing thermally-driven martensitic transformation, then triggering and controlling the extent of deformation-driven martensitic transformation by controlling thermal strain.

Melt pool modelling predicted that the full range of SLM build conditions would have solidification rates in the range 10^4 – 10^6 K s^{-1} , resulting in cellular solidification with $\lambda_1 < 5 \mu\text{m}$. This was confirmed by the experimental microstructures observed by SEM even at very high energy density (Fig. 7). It is also consistent with the microstructures reported for SLM-built 17-4PH and other steels [7,29,47]. In addition to the fine cell size, all build conditions showed comparable grain sizes of 10–20 μm , with no observable trend in grain size with increasing energy density (Fig. 8).

The model also predicted that any in-situ heat treatment caused by the addition of subsequent hatches and layers would be too short to cause coarsening of this structure. This was confirmed by SEM images

through the depth which showed no coarsening of the solidification cells even in the highest energy density condition (Supplementary Fig. 5).

It had been predicted that, in the absence of a secondary driving force (e.g. strain), the grain and solidification cell size of SLM-built 17-4PH would be sufficiently fine to suppress thermally-activated martensite and give a fully metastable austenite structure at room temperature. The role of solidification cells in suppressing thermal M_s was based on literature reporting martensite growth being stopped by dense dislocation walls comparable with the cell boundaries.

The low energy density (S5) condition was predicted to have the lowest thermal strain, and was therefore likely to have the highest levels of retained austenite. This was confirmed by VSM to have <0.5 wt% martensite in the as-built condition, and have a paramagnetic response to an applied field (Fig. 2). Separately, the XRD showed a majority austenitic structure with very low martensite intensity (Fig. 5). This demonstrated that a grain size of 10–20 μm , combined with a solidification cell size below 2 μm , was capable of fully suppressing the thermally-driven martensitic transformation in this composition of 17-4PH.

To achieve a magnetically graded material it was also necessary to create material with a controllable proportion of ferromagnetic martensite. All build conditions were predicted to have comparable solidification cell sizes, so thermal martensite would be suppressed in all cases. Increasing energy density was predicted to cause an increase in thermal strain, although without calibration it was not possible to predict if it would be sufficient to drive controllable martensitic transformation through TRIP.

The experimental data showed the high energy density condition to have 29% ferromagnetic martensite, indicating that the magnitude of thermal strain had been sufficient to trigger transformation. Further,



Fig. 9. Synchronous motor application. a) Schematic of rotor design showing flux guides and support struts. b) SLM-built, magnetically graded rotor built into demonstrator motor. c) Output measured from demonstrator motor at 400 rpm.

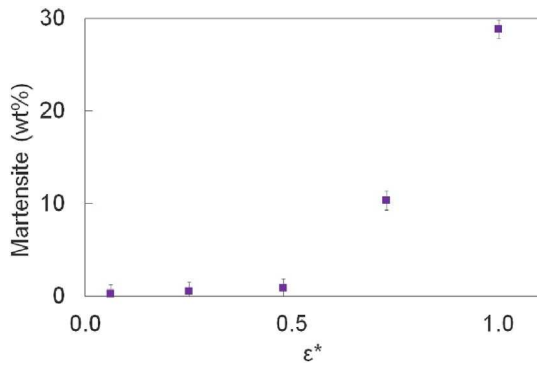


Fig. 10. Martensite phase fraction from VSM against normalised thermal deformation parameter. Error bars show standard error.

the intermediate conditions showed increasing martensite with increasing thermal strain (Fig. 10), confirming that variation in thermal strain achieved by changing build parameters was capable of controlling the extent of transformation.

In addition to the effect of energy density, the thermal strain parameter predicted that sample geometry would influence thermal strain through a combination of the deposition time (dependent on surface area and sample height) and the rigidity of the sample. If the martensite was deformation-driven, there should be a correlating change in martensite content with geometry and build height. Whereas, if it was thermally-driven, transforming on cooling after solidification, samples with the same build parameters would be expected to have consistent phase fraction, and there should be no variation with build height.

There is literature showing that thermal strain in additively manufactured samples increases with distance from the baseplate [13,17]. Feritscope data showed martensite content for all high energy density (S1) samples increasing from 0 wt% to 30 wt% with increasing distance from the build plate in the S1 sample (Fig. 3). This pattern in martensite content, correlating with the pattern of thermal strain in AM components, is further evidence that the martensite has been triggered by deformation.

The change in martensite content with height was steepest through the first 5 mm, with one sample '2 × 10' saturating at 30 wt% after 10 mm, while the others still increased but more slowly. This can be explained by the baseplate increasing rigidity for the early layers, resisting deformation. As the build surface moves upwards, the baseplate has a reduced effect, so thermal strain increases. After a certain number of layers, the baseplate no longer influences rigidity because the melt pool is too far away.

Each geometry sample also showed different levels of martensite, which would not be expected were the martensite thermally driven on cooling after solidification. There was an indication that sample area and aspect ratio were both important, with the '20 × 10' and '10 × 5' samples showing similar trends in martensite content with build height, while the '10 × 10' sample showed a much slower increase. A larger sample area would have a longer deposition time and therefore more heat input, which would be expected to increase thermal strain, but would be more rigid so better able to resist deformation.

The graded cuboid (Fig. 1a), manufactured from blocks of each energy density condition build concurrently, showed a magnetically graded response to a handheld magnet. This demonstrated that the conditions, shown to have different magnetic responses when built individually, could be successfully combined to create an in-situ graded structure. The high and low energy density build conditions were then used to create an SLM-built, magnetically graded rotor, which was successfully tested in a demonstrator motor.

An unexpected observation was the split austenite peaks observed in the XRD data (Fig. 5). This is currently under investigation, but it is

believed this may be due to carbon partitioning from the supersaturated martensite in a similar manner to that observed with bainitic ferrite [48,49].

6. Conclusions

- For 17-4PH, the rapid solidification associated with SLM drives a characteristic microstructure of small grains (10–20 μm) containing elongated solidification cells, <2 μm in diameter. This was shown to be consistent both with changing energy density and through sample depth.
- At low energy density, in the absence of thermal strain, this microstructure was sufficiently fine to suppress the thermally-driven martensitic transformation in this composition of 17-4PH, resulting in a paramagnetic, fully austenitic material.
- At higher energy density, while the microstructure still suppressed thermal martensite, the increased thermal strain was sufficient to trigger deformation martensite. The martensite phase fraction was shown to increase with increasing thermal strain.
- The martensite content was also shown to be dependent on the increase of thermal strain with build height, and the effect of component geometry.
- This effect was exploited to build an in-situ magnetically graded cuboidal sample, and a magnetically graded motor which was run in a demonstrator motor.

Funding

This research was funded by the Engineering and Physical Sciences Research Council (EPSRC) under award reference 1686001.

CRediT authorship contribution statement

Felicity S.H.B. Freeman: Data curation, Formal analysis, Investigation, Methodology, Software, Validation, Writing - original draft. **Alex Lincoln:** Formal analysis. **Jo Sharp:** Formal analysis. **Al Lambourne:** Conceptualization, Formal analysis, Investigation, Methodology, Supervision, Writing - review & editing. **Iain Todd:** Conceptualization, Funding acquisition, Project administration, Resources, Supervision, Writing - review & editing.

Acknowledgements

This research was funded by the Engineering and Physical Sciences Research Council (EPSRC) under award reference 1686001. Prof. Dan Allwood and Dr. René Dost (University of Sheffield) advised on magnetic characterisation. Dr. Jason Ede, Dr. Mark Sweet, Dr. Stephen Forrest & Dr. Keir Wilkie (University of Sheffield) supported the testing of the magnetically graded rotor. Dr. Mike Croucher (University of Sheffield) advised with the creation of the Matlab model.

Author contributions

F.F. designed the experiment, built the samples, created the melt pool model and performed the XRD and Feritscope characterisation. A. Lincoln performed the VSM measurements and advised on interpretation of VSM data. A. Lambourne conceived the concept of a magnetically graded material for synchronous motors, obtained the demonstrator motor and organised the testing. J. Sharp obtained the SEM images. I.T. and F.F. and A. Lambourne discussed the results and F.F. wrote the manuscript.

Conflict of interest

The authors declare no competing financial interest.

Data availability

The datasets generated during and/or analysed during the current study are available from the corresponding author on reasonable request.

Appendix A. Relationship between prior austenite grain size and martensite start temperature [9]

$\Delta M_s = \frac{1}{b} \ln \left[\frac{1}{V_\gamma} \left\{ \exp \left(-\frac{\ln(1-f)}{m} \right) - 1 \right\} + 1 \right]$		
ΔM_s	Change in martensite start temperature	
L_γ	Diameter of austenite grain	μm
V_γ	Volume of austenite grain	$\frac{4}{3} \pi (L_\gamma/2)^3$ μm^3
m	Aspect ratio of martensite plate	0.05
f	Fraction martensite	0.01
a	Constant	1.57×10^{-21} μm^3
b	Constant	0.253

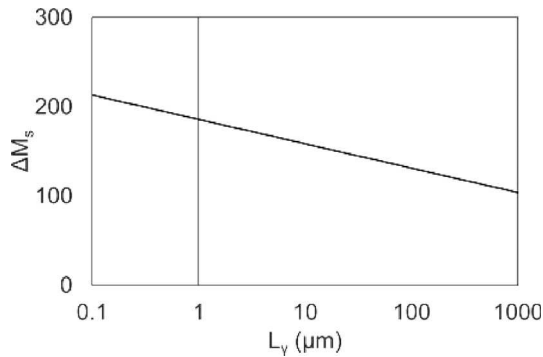


Fig. 11. Relationship between prior austenite grain size and suppression of thermally-driven martensite start temperature.

Appendix B. Supplementary data

Supplementary data to this article can be found online at <https://doi.org/10.1016/j.matdes.2018.11.011>.

References

- [1] C.N. Hsiao, C.S. Chiou, J.R. Yang, Aging reactions in a 17-4 PH stainless steel, *Mater. Chem. Phys.* 74 (2002) 134–142.
- [2] F. Christien, M.T.F. Telling, K.S. Knight, A comparison of dilatometry and in-situ neutron diffraction in tracking bulk phase transformations in a martensitic stainless steel, *Mater. Charact.* 82 (2013) 50–57.
- [3] D.P. Koistinen, R.E. Marburger, A general equation prescribing the extent of the austenite-martensite transformation in pure iron-carbon alloys and plain carbon steels, *Acta Metall.* 7 (1959) 59–60.
- [4] L. Facchini, et al., Metastable austenite in 17-4 precipitation-hardening stainless steel produced by selective laser melting, *Adv. Eng. Mater.* 12 (2010) 184–188.
- [5] W.E. Luecke, J.A. Slotwinski, Mechanical properties of austenitic stainless steel made by additive manufacturing, *J. Res. Natl. Inst. Stand. Technol.* 119 (2014) 398–418.
- [6] L.E. Murr, et al., Microstructures and properties of 17-4 PH stainless steel fabricated by selective laser melting, *J. Mater. Res. Technol.* 1 (2012) 167–177.
- [7] H.K. Rafi, D. Pal, N. Patil, T.L. Starr, B.E. Stucker, Microstructure and mechanical behavior of 17-4 precipitation hardenable steel processed by selective laser melting, *J. Mater. Eng. Perform.* 23 (2014) 4421–4428.
- [8] H. Gu, et al., Influences of energy density on porosity and microstructure of selective laser melted 17-4PH stainless steel, *Solid Freeform Fabrication Symposium 2013*, pp. 474–489.
- [9] H.-S. Yang, H.K.D.H. Bhadeshia, Austenite grain size and the martensite-start temperature, *Scr. Mater.* 60 (2009) 493–495.
- [10] A. García-Junceda, C. Capdevila, F.G. Caballero, C.G. de Andrés, Dependence of martensite start temperature on fine austenite grain size, *Scr. Mater.* 58 (2008) 134–137.
- [11] S. Takaki, K. Fukunaga, J. Syarif, T. Tsuchiyama, Effect of grain refinement on thermal stability of metastable austenitic steel, *Mater. Trans.* 45 (2004) 2245–2251.
- [12] W. Kurz, R. Trivedi, Rapid solidification processing and microstructure formation, *Mater. Sci. Eng. A* 179 (1994) 46–51.
- [13] R.J. Deffley, Development of Processing Strategies for the Additive Layer Manufacture of Aerospace Components in Inconel 718, University of Sheffield, 2012.
- [14] D. Buchbinder, H. Schleifenbaum, S. Heidrich, J. Bültmann, High power selective laser melting (HP SLM) of aluminum parts, *Phys. Procedia* 12 (2011) 271–278.
- [15] Y. Inokuti, B. Cantor, Splat-quenched Fe-Ni alloys, *Scr. Metall.* 10 (1976) 655–659.
- [16] A.L. Schaeffler, Constitution diagram for stainless steel weld metal, *Met. Prog.* 56 (1949) 680.
- [17] P. Mercelis, J.P. Kruth, Residual stresses in selective laser sintering and selective laser melting, *Rapid Prototyp. J.* 12 (2006) 254–265.
- [18] P. Vora, K.A. Mumtaz, I. Todd, N. Hopkinson, AlSi12 in-situ alloy formation and residual stress reduction using anchorless selective laser melting, *Addit. Manuf.* (2015) <https://doi.org/10.1016/j.addma.2015.06.003>.
- [19] D.C. Hofmann, et al., Developing gradient metal alloys through radial deposition additive manufacturing, *Sci. Rep.* 4 (2015) 5357.
- [20] K.A. Mumtaz, N. Hopkinson, Laser melting functionally graded composition of Waspaloy and Zirconia powders, *J. Mater. Sci.* 42 (2007) 7647–7656.
- [21] T.H. Fang, W.L. Li, N.R. Tao, K. Lu, Revealing extraordinary intrinsic tensile plasticity in gradient nano-grained copper, *Science* (80-.) 331 (2011) 1587–1590.
- [22] Y. Wei, et al., Evading the strength-ductility trade-off dilemma in steel through gradient hierarchical nanotwins, *Nat. Commun.* 5 (2014) 2588–2604.
- [23] S.D. Calverley, G.W. Jewell, R.J. Saunders, Aerodynamic losses in switched reluctance machines, *IEE Proc. Electr. Power Appl.* 147 (2000) 443.
- [24] H. Hofmann, S.R. Sanders, High-speed synchronous reluctance machine with minimized rotor losses, *IEEE Trans. Ind. Appl.* 36 (2000) 531–539.
- [25] A. Duke, Brushless Doubly-fed Reluctance Machines for Aerospace Electrical Power Generation Systems, University of Sheffield, 2015.
- [26] B.J. Chalmers, L. Musaba, Design and field-weakening performance of a synchronous reluctance motor with axially-laminated rotor, *IAS '97. Conference Record of the 1997 IEEE Industry Applications Conference Thirty-Second IAS Annual Meeting*, vol. 1, IEEE 1997, pp. 271–278.
- [27] F.B. Reiter, T.L. Stuart, S.M. Clase, B.D. Beard, Method of Making a Powder Metal Rotor for a Synchronous Reluctance Machine, 2004 13.
- [28] K. Saeidi, X. Gao, F. Lofaj, L. Kvetková, Z.J. Shen, Transformation of austenite to duplex austenite-ferrite assembly in annealed stainless steel 316L consolidated by laser melting, *J. Alloys Compd.* 633 (2015) 463–469.
- [29] E.A. Jägle, P.-P. Choi, J. Van Humbeeck, D. Raabe, Precipitation and austenite reversion behavior of a maraging steel produced by selective laser melting, *J. Mater. Res.* 29 (2014) 2072–2079.
- [30] R. Mertens, et al., Influence of powder bed preheating on microstructure and mechanical properties of H13 tool steel SLM parts, *Phys. Procedia* 83 (2016) 882–890.
- [31] V.D. Divya, et al., Microstructure of selective laser melted CM247LC nickel-based superalloy and its evolution through heat treatment, *Mater. Charact.* 114 (2016) 62–74.
- [32] Y.M. Wang, et al., Additively manufactured hierarchical stainless steels with high strength and ductility, *Nat. Mater.* 17 (2018) 63–70.
- [33] I. Gilath, J.M. Signamarcheix, P. Bensussan, A comparison of methods for estimating the weld-metal cooling rate in laser welds, *J. Mater. Sci.* 29 (1994) 3358–3362.
- [34] M. El-Bealy, B.G. Thomas, Prediction of dendrite arm spacing for low alloy steel casting processes, *Metall. Mater. Trans. B Process Metall. Mater. Process. Sci.* 27 (1996) 689–693.
- [35] H. Jacobi, K. Schwerdtfeger, Dendrite morphology of steady state unidirectionally solidified steel, *Metall. Trans. A* 7 (1976) 811–820.
- [36] W. Kurz, D.F. Fisher, Fundamentals of Solidification, Trans Tech Publications, 1989.
- [37] T.W. Eagar, N.S. Tsai, Temperature fields produced by traveling distributed heat sources, *Weld. J.* 62 (1983) 346–355.
- [38] W.E. King, et al., Observation of keyhole-mode laser melting in laser powder-bed fusion additive manufacturing, *J. Mater. Process. Technol.* 214 (2014) 2915–2925.
- [39] M. Thomas, G.J. Baxter, I. Todd, Normalised model-based processing diagrams for additive layer manufacture of engineering alloys, *Acta Mater.* 108 (2016) 26–35.
- [40] J. Trapp, A.M. Rubenchik, G. Guss, M.J. Matthews, In situ absorptivity measurements of metallic powders during laser powder-bed fusion additive manufacturing, *Appl. Mater. Today* 9 (2017) 341–349.
- [41] T. Shigeta, A. Takada, H. Terasaki, Y.-I. Komizo, The effects of ausforming on variant selection of martensite in Cr–Mo steel, *Q. J. Japan Weld. Soc.* 31 (2013) 178–182.
- [42] M. Griffith, et al., Understanding thermal behavior in the LENS process, *Mater. Des.* 20 (1999) 107–113.
- [43] W.J. Sames, K.A. Unocic, R.R. Dehoff, T. Lolla, S.S. Babu, Thermal effects on microstructural heterogeneity of Inconel 718 materials fabricated by electron beam melting, *J. Mater. Res.* 29 (2017) 1920–1930.
- [44] T. Mukherjee, J.S. Zuback, A. De, T. Debroy, Printability of alloys for additive manufacturing, *Sci. Rep.* 6 (2016).
- [45] B.D. Cullity, C.D. Graham, Introduction to Magnetic Materials, IEEE/Wiley, 2009.
- [46] S.S.M. Tavares, J.M. Pardo, T.R.B. Martins, M.R. da Silva, Influence of sulfur content on the corrosion resistance of 17-4PH stainless steel, *J. Mater. Eng. Perform.* 26 (2017) 2512–2519.
- [47] K. Saeidi, X. Gao, Y. Zhong, Z.J. Shen, Hardened austenite steel with columnar sub-grain structure formed by laser melting, *Mater. Sci. Eng. A* 625 (2015) 221–229.
- [48] S.S. Babu, et al., In-situ observations of lattice parameter fluctuations in austenite and transformation to bainite, *Metall. Mater. Trans. A* 36A (2005) 3281–3289.
- [49] H.J. Stone, et al., Synchrotron X-ray studies of austenite and bainitic ferrite, *Proc. R. Soc. A* 464 (2008) 1009–1027.